

# Cysteine-Grafted Cu MOF/ZnO/PANI Nanocomposite for Nonenzymatic Electrochemical Sensing of Dopamine

Mariam Basharat, Zakir Hussain,\* Dooa Arif, and Waheed Miran

Cite This: *ACS Omega* 2024, 9, 49545–49556

Read Online

ACCESS |



Metrics &amp; More

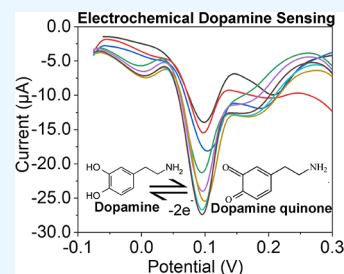


Article Recommendations



Supporting Information

**ABSTRACT:** Electrochemical sensing has shown great promise in monitoring neurotransmitter levels, particularly dopamine, essential for diagnosing neurological illnesses like Parkinson's disease. Such techniques are easy, cost-effective, and extremely sensitive. The present investigation discusses the synthesis, characterization, and potential use of a cysteine-grafted Cu MOF/ZnO/PANI nanocomposite deposited on the modified glassy carbon electrode surface for nonenzymatic electrochemical sensing of dopamine. The synthesized nanocomposite was confirmed through X-ray diffraction, Fourier transform infrared, Raman, and scanning electron microscopy characterization techniques. Additionally, electrochemical analysis was conducted using cyclic voltammogram, differential pulse voltammetry, and chronoamperometry. The process was determined to be the diffusion-controlled oxidation of dopamine. Dopamine underwent spontaneous adsorption on the electrode surface through an electrochemically reversible mechanism. Despite various biological interfering factors, the nonenzymatic electrochemical sensor demonstrated a remarkable level of selectivity toward dopamine. Cysteine-grafted Cu MOF/ZnO/PANI produced the lowest dopamine detection limit, at 0.39  $\mu\text{M}$ , and the sensitivity was observed as 122.57  $\mu\text{A}\text{mM}^{-1}\text{cm}^{-2}$ . Results have demonstrated that enhanced catalytic and conductive properties of MOFs, combined with nanostructured materials, are the primary factors affecting the sensor's performance.



## 1. INTRODUCTION

The catecholamine neurotransmitter known as dopamine (DA) was first identified in 1957 by Carlsson.<sup>1</sup> The endocrine, central nervous, renal, and cardiovascular systems are all affected by this substance, which plays a crucial role in regulating several physiological processes, including behavior, mood, memory, learning, and mental cognition.<sup>2</sup> Multiple disorders, such as Depression, Parkinson's disease, Attention Deficit Hyperactivity Disorder (ADHD), Alzheimer's disease, and Schizophrenia can be attributed to inadequate levels of DA.<sup>3</sup> Hence, developing a simple, economical, and responsive technique for measuring DA levels in the human body is crucial. Various methods, including calorimetric fluorescence, spectrophotometry, chemiluminescence, and high-performance liquid chromatography (HPLC), are now employed to detect DA.<sup>4</sup> Nevertheless, these techniques are costly, arduous, time-consuming, and need expensive analytical reagents, delaying early disease detection.<sup>5</sup> Hence, the electrochemical method is the most direct, uncomplicated, and economical approach for detecting DA. The measurement of DA electrochemically reveals that biological substances, specifically uric acid (UA), ascorbic acid (AA), and glucose (Glu), have comparable reduction and oxidation potentials.<sup>6</sup> Several materials have been developed to modify the electrode surface to enhance the selectivity toward DA.

Metal–organic frameworks (MOFs) represent a novel category of extremely crystalline nanoporous materials formed through coordination bonds that connect metal ions or clusters to their organic ligands or serve as intermediaries between the

metal ions or clusters and the organic ligands. In recent years, metal–organic frameworks (MOFs) have garnered heightened interest due to their remarkable attributes, including high crystallinity, adjustable pore structure, extensive specific surface area, and customizable chemical characteristics. These notable qualities render them adaptable for many applications, including electrocatalysis, gas adsorption, controlled drug release, and energy storage.<sup>7,8</sup> Nevertheless, pristine MOFs are unsuitable for fabricating electrochemical sensors owing to their inherent low conductivity and electrochemical instability. Metal–organic frameworks (MOFs) are frequently combined with conductive materials, particularly carbon-based substances, to resolve this issue. MOFs-based composites preserve their inherent porous architectures and extensive specific surface areas while significantly improving electrical conductivity and electrochemical stability.<sup>9</sup> Cu-MOF, also known as CuBTC or HKUST-1, is a well-studied material with advantages such as simple preparation, numerous metal sites, and a large surface area.<sup>10</sup> Cu MOF was selected as an alternative MOF because of its exceptional features that meet the criteria for efficient sensing. Cu MOF exhibits excellent

Received: August 13, 2024

Revised: October 22, 2024

Accepted: October 30, 2024

Published: December 3, 2024



conductivity, crucial for efficient electron transfer in electrochemical reactions, making it particularly effective in redox-based sensors. The copper ions in Cu MOF exhibit superior catalytic activity, improving the sensor's sensitivity and selectivity. Furthermore, Cu MOF demonstrates a substantial surface area and porosity, facilitating enhanced interaction with analytes and augmenting the sensor's overall efficacy. In addition, the capacity of Cu MOF to create composites with ZnO and PANI significantly augments its conductivity and stability in electrochemical settings, resulting in enhanced sensing performance. These composites use the distinct characteristics of each material, including the elevated electron mobility of ZnO and the conductive qualities of PANI, culminating in a synergistic effect that enhances sensor performance. The selection of Cu MOF over other MOFs is frequently motivated by its superior electrochemical activity, adaptability in composite synthesis, and compatibility with diverse sensing platforms, as evidenced by research highlighting its improved efficacy in particular sensing applications.<sup>11,12</sup>

Additionally, materials such as conductive polymers (e.g., polypyrrole and polythiophene) have also become increasingly significant in several fields due to their potential applications.<sup>13–16</sup> Polyaniline (PANI), a polymer with inherent conductivity, holds significant importance due to its diverse redox states, exceptional stability, cost-effectiveness as a monomer, simplicity in synthesis, and extensive utilization in various fields such as electronics, electrochromic devices, separating membranes, anticorrosion treatments, and sensors.<sup>17–20</sup>

Metal oxides, including ZnO, TiO<sub>2</sub>, and CuO, exhibit nanostructured forms with increased surface areas, increasing analyte adsorption and markedly enhancing sensor sensitivity. The enhanced surface-to-volume ratio of metal oxides facilitates additional reactive sites for electron transfer processes, leading to diminished detection limits.<sup>21</sup> Metal oxides have chemical and thermal stability, rendering them suitable for electrochemical sensing across many environmental conditions. The stability of metal oxides enhances the long-term functionality of sensors, particularly under difficult or extreme conditions.<sup>22</sup> Numerous metal oxides are available and cost-effective to manufacture, particularly in contrast to noble metals or other advanced materials. This attribute makes them economically feasible for extensive sensor manufacturing.<sup>23</sup> Metal oxides have adjustable electrical characteristics, including broad bandgaps, which can be altered via doping or the formation of composite materials. This facilitates the optimization of the sensor's performance based on the target analyte.<sup>24</sup> Due to their intrinsic characteristics, metal oxides, namely zinc oxide (ZnO), boost the sensitivity and selectivity in identifying biomolecules such as DA. The nanostructured metal oxides have notable characteristics such as a substantial specific surface area, catalytic efficiency, and robust adsorption capability. These properties are critical in developing electrochemical sensors and biosensors with exceptional sensitivity. These sensors are widely utilized in various fields, such as medical diagnostics, pharmaceutical analysis, and environmental monitoring. They are essential for accurately detecting analytes like DA.<sup>25</sup> However, they also have limitations, such as inadequate selectivity and sensitivity. Nanomaterials possess many physical characteristics that improve their catalytic efficiency, such as a high surface area-to-volume ratio, quantum size effects, and surface imperfections, which collectively

increase the number of active sites and reduce activation energy for reactions.<sup>26</sup> Moreover, their capacity to enable fast charge transfer and reveal catalytically active crystal aspects enhances their efficiency.<sup>26,27</sup> In specific nanomaterials, plasmonic effects can augment photocatalytic processes by producing hot electrons, enhancing catalytic activity when exposed to light.<sup>28</sup>

Also, incorporating amino acids, such as cysteine, in developing electrochemical sensors for DA shows promise due to the distinctive binding interactions exhibited by such biomolecules. The thiol group in cysteine enables it to establish robust covalent interactions with specific functional groups in DA. This relationship facilitates an enhanced and precise sensing mechanism, vital in differentiating DA from other analogous chemicals found in intricate biological specimens. The possible binding of the thiol group in cysteine to the catechol structure in DA can enhance the electrochemical signal by promoting an efficient electron transfer pathway. This approach improves the sensor's sensitivity and enhances its selectivity, which is crucial in achieving precise DA measurements. Incorporating amino acids, such as cysteine, into electrochemical sensing platforms signifies a notable progression in creating biosensors with enhanced specificity and sensitivity for detecting neurotransmitters. Therefore, the main focus of the present investigation is integrating the above-discussed materials in exploring the synergistic effect and fabricating a highly sensitive and selective sensing system for detecting DA.<sup>29</sup>

This study focused on developing a novel composite material comprising cysteine-grafted Cu-MOF/ZnO/PANI and fabricating a sensing surface on a glassy carbon electrode (GCE) for dopamine (DA) detection.

## 2. MATERIALS AND METHODS

**2.1. Materials.** Urea, L-Cysteine hydrochloride Monohydrate, 1,3,5-benzene tricarboxylic acid (BTC) and copper(II) nitrate trihydrate (Cu(NO<sub>3</sub>)<sub>2</sub>·3H<sub>2</sub>O, methanol (≥99.8%), and distilled aniline (≥20%). (L+)-Ascorbic acid, Ammonium persulfate (APS), and (D+)-Glucose anhydrous were acquired from Merck, Germany. The HCl (≥40%) and (DMF) *N,N*-dimethylformamide (5%) were acquired from Honeywell (USA) and AnalaR (UK), respectively, while ethanol (40%) was procured from the RCI Labscan (Thailand). The dopamine hydrochloride (≥98%) was obtained from Solar Bio (China), and NaOH and zinc acetate were obtained from Daejung Chemicals (S. Korea). All chemicals were utilized without any additional purification or treatment.

**2.2. Synthesis of Cu MOF (HKUST-1, Cu-BTC, or MOF-119).** Cu MOF was synthesized by a hydrothermal method.<sup>30</sup> Briefly, in 45 mL of 1:1 solution of absolute ethanol/*N,N*-dimethylformamide (DMF), 1.50 g (7.1 mM) of 1,3,5-benzene tricarboxylic acid were dissolved, and the mixture was allowed to stir at the room temperature for 20 min. Subsequently, 3.11 g (16.58 mM) of copper(II)nitrate trihydrate was added to 22.5 mL deionized water, and stirring continued for an additional 20 min at room temperature. The mixture was then shifted to a Teflon-lined stainless-steel 100 mL autoclave and heated at 120 °C for 24 h. After the autoclave was cooled to room temperature, the obtained blue crystals were filtrated and rinsed with deionized water and ethanol. The material obtained was dried in a vacuum oven at 60 °C overnight. Following the postmodification of the prepared Cu MOF with cysteine,<sup>31,32</sup> 0.372 g (3.07 mM) of cysteine crystals were fully

ground, dissolved in absolute ethanol at 50 °C, and left for continuous stirring for 1 h. The synthesized Cu MOF was introduced into the solution and subjected to constant stirring for 24 h on a hot plate maintained at 50 °C. The residual solution was then repeatedly rinsed with ethanol at room temperature, and the obtained powder was dried in a vacuum oven at 60 °C overnight.

**2.3. Synthesis of Polyaniline (PANI).** Polyaniline nanofibers (PANI) were synthesized using the literature procedure.<sup>33</sup> In an ice bath, 3 mL of aniline monomer was added to 25 mL of 1 M HCl solution in a round-bottom flask and stirred for 25 min. Subsequently, 2.5 g (0.01 M) of APS was added to 25 mL of 1 M HCl solution, stirred for 20 min, and added dropwise to the aniline solution. The stirring continued for another 4 h, then polymerizing the mixture in the refrigerator for 24 h. Finally, the obtained precipitate was washed and filtered many times with ethanol and deionized water, and the obtained polymer was dried in a vacuum oven at 60 °C overnight.

**2.4. Synthesis of Cu MOF and Polymer Composite.** Synthesis of the composite was carried out using an already published method.<sup>34</sup> Briefly, a 33.2 g (0.158 M) solution of trimesic acid was prepared in a mixture containing 11.25 mL of DMF and 11.25 mL of ethanol. Simultaneously, 87.7 g (0.468 M) of copper nitrate trihydrate was prepared in 11.25 mL of deionized water. Subsequently, 0.1 g (0.001 mM) of the above-prepared polymer was added to this mixture and stirred for 5 min. Finally, both solutions were combined and stirred for 15 min at room temperature. The mixture was transferred to a hydrothermal reactor lined with Teflon and kept at 100 °C for 10 h. The resulting product was filtrated and rinsed with ethanol thrice to eliminate any remaining unreacted substances. The acquired sample was dried overnight in a vacuum oven at 50 °C. The material was homogenized and stored in a closed vial.

**2.5. Postsynthetic Modification of Cu MOF/PANI with Cysteine.** The above-prepared composite was functionalized with cysteine using a method reported previously.<sup>31,32</sup> Briefly, 0.372 g (3.07 mM) of cysteine crystals were fully ground, dissolved in absolute ethanol at 50 °C, and left for continuous stirring for 1 h, followed by the addition of Cu MOF/PANI into the solution and stirring for 24 h on a hot plate at 50 °C. After the solution was cooled to room temperature, the remaining solution was washed with ethanol many times, and the obtained powder was dried in a vacuum oven at 60 °C overnight.

**2.6. Synthesis of ZnO Nanoparticles.** ZnO nanoparticles (NPs) were synthesized using the method described in the literature with certain modifications.<sup>35</sup> Briefly, zinc acetate solution was prepared by dissolving 4.4 g (0.023 M) of  $\text{Zn}(\text{CH}_3\text{CO}_2)_2 \cdot 2\text{H}_2\text{O}$  in 20 mL of distilled water, and it was added dropwise with NaOH solution to maintain the pH at 4.6, followed by stirring for 12 h and centrifuged for 30 min at 5000 rpm. The obtained material was washed thrice with ethanol and water to remove impurities, and the obtained product was dried in an oven at 50 °C for 3 h. Subsequently, the material was calcined at 350 °C for 2 h to obtain ZnO NPs.

**2.7. Synthesis of the Cu MOF/ZnO Nanocomposite.** For the synthesis of the above nanocomposite, a 33.2 g (0.158 M) solution of trimesic acid was prepared in a mixture of 11.25 mL of DMF and 11.25 mL of ethanol. Simultaneously, an 87.7 g (0.468 M) solution of copper nitrate trihydrate was prepared in 11.25 mL of DI water, followed by adding 0.1 g (0.001 M)

of the ZnO NPs into the copper nitrate mixture and stirring for 5 min. Following the procedure, both mixtures were combined, stirred for 15 min at room temperature, transferred to a hydrothermal reactor lined with Teflon, and kept the same at 100 °C for 10 h. The resulting product was filtrated and rinsed with DI water and ethanol three times to eliminate any remaining unreacted substances. The acquired material was dried overnight in a vacuum oven at 50 °C.

**2.8. Postsynthetic Modification of PANI with the Cu MOF/ZnO Nanocomposite.** The above product was prepared by using an already-published method.<sup>36</sup> Briefly, in a round-bottomed flask, 3 mL of aniline monomer was added in 25 mL of 1 M HCl solution and stirred for 25 min at 50 °C followed by the addition of 0.05 g (0.0727 mM) of Cu MOF/ZnO nanocomposite to this solution and stirring continued for 25 min to obtain a homogeneous mixture. Following the procedure, a solution of 2.5 g (0.01 M) of APS in 25 mL of 1 M HCl was added dropwise to the above mixture, and stirring continued for 4 h at 50 °C. After removing the excess solvent by drying it in an oven, the obtained precipitate was washed and filtered many times with ethanol and DI water. The material was finally dried overnight in a vacuum oven at 60 °C.

**2.9. Postsynthetic Modification of the Cu MOF/ZnO/PANI Nanocomposite with Cysteine.** The synthesized Cu MOF/ZnO/PANI was functionalized with cysteine by employing previously reported methods.<sup>31,32</sup> Briefly, 0.372 g (3.07 mM) of cysteine crystals were fully ground, dissolved in absolute ethanol at 50 °C, and stirred for 1 h. Then, synthesized Cu MOF/ZnO/PANI was added to this solution, and stirring continued for another 24 h at 50 °C. Finally, the solution was cooled to room temperature, and the mixture was washed with ethanol thrice to obtain powder, which was further dried overnight in a vacuum oven at 60 °C.

**2.10. Preparation of the Modified Electrode.** Before conducting measurements, the glassy carbon electrode (GCE) was subjected to a polishing procedure involving alumina slurry on a cloth polishing pad. The process was performed by moving in a figure-eight pattern to guarantee a uniformly polished surface of the electrode. Afterward, the tip of the electrode was placed into a solution of 100% ethanol and distilled water in a small glass vial with a volume of 15 mL. The solution was subsequently exposed to ultrasonication briefly to get a pristine and lustrous electrode surface. To create the slurry, 2 mg of the sample material was evenly distributed in 150  $\mu\text{L}$  of ethanol and subjected to sonication for 15 to 20 min. Subsequently, 10  $\mu\text{L}$  of Nafion, employed as a binding agent, was introduced into the suspension, and the amalgamation was subjected to sonication for an extra 30 min to guarantee a consistent suspension. The prepared slurry was ultimately carefully applied onto the working electrode using drop-casting. Subsequently, it was dried at room temperature to obtain modified GCE.

## 3. RESULTS AND DISCUSSION

**3.1. Scanning Electron Microscopy.** Scanning electron microscopy (SEM) was used to analyze the surface morphological examinations of the as-synthesized samples. Figure 1 demonstrates the morphological characteristics of Cu MOF, Cys/Cu MOF/PANI, Cu MOF/PANI, Cys/Cu MOF/PANI, ZnO, Cu MOF/ZnO, Cu MOF/ZnO/PANI, and Cys/Cu MOF/ZnO/PANI nanocomposite. Figure 1A vividly depicts the porous octahedral form of the Cu MOF crystals. The Cu MOF samples exhibited crystal sizes ranging from 5 to

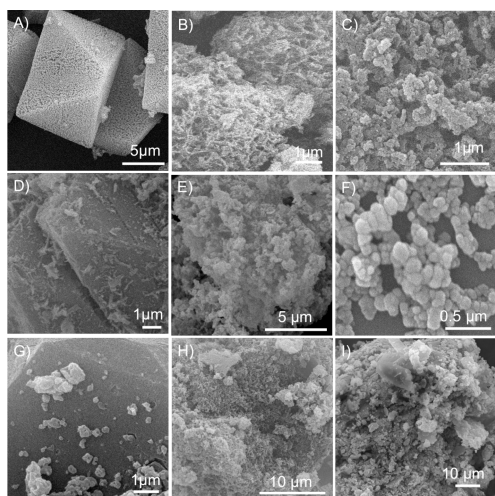


**Figure 1.** SEM results of (A) Cu MOF, (B) Cys/Cu MOF composite, (C) PANI nanotubes, (D) Cu MOF/PANI composite, (E) Cys/Cu MOF/PANI composite, (F) ZnO NPs, (G) Cu MOF/ZnO composite, (H) Cu MOF/ZnO/PANI composite, and (I) Cys/Cu MOF/ZnO/PANI nanocomposite.

10  $\mu\text{m}$ , with no signs of aggregation. The Cu MOF samples' morphology in their original state exhibited a similar structure in the SEM pictures previously reported.<sup>37</sup> The SEM pictures of the Cu MOF functionalized with cysteine revealed elongated spindle-shaped crystals of cysteine, as depicted in Figure 1B. However, the structural characteristics of the original Cu MOF are not effectively maintained following the addition of cysteine functional groups, as demonstrated.<sup>32</sup> The uniform growth of nanotubes with branched geometry and an average diameter ranging from 60 to 100 nm is shown by the neat PANI in Figure 1C. The nanotubes appear porous and agglomerated.<sup>38</sup> The PANI/MOF composite displayed more refined morphological characteristics than pure PANI. Because there was less PANI in the composite, it is also evident that the MOF crystal structures are visible, as shown in Figure 1D.<sup>39</sup> The Cu MOF surface exhibited a consistent distribution of spindle-shaped cysteine crystals and PANI nanotubes, as depicted in Figure 1E. ZnO NPs exhibit a roughly spherical form and homogeneous morphology (Figure 1F) with particle size ranging from 60 to 80 nm. Lack of simultaneous control over particle size, shape, and size distribution is the main obstacle for making ZnO NPs.<sup>40</sup> Similarly, Figure 1G illustrates the deposition of ZnO NPs onto the MOF surface, which is nearly spherical. The composition of ZnO distribution on the MOF surface is nonuniform. Figure 1H displays spherical ZnO nanoparticles and PANI nanotubes onto the MOF surface; nevertheless, the Cu MOF's shape did not remain intact. The significantly high abundance of PANI overshadowed the almost spherical ZnO NPs (Figure 1I).

**3.2. X-ray Diffraction Analysis.** In the X-ray diffraction (XRD), intensities were measured across the range of  $10^\circ$  to  $80^\circ$ . Figure 2 demonstrates the reflections due to Cu MOF, Cys/Cu MOF/PANI, Cu MOF/PANI, Cys/Cu MOF/PANI, ZnO, Cu MOF/ZnO, Cu MOF/ZnO/PANI, and Cys/Cu MOF/ZnO/PANI nanocomposite. The XRD pattern of the Cu MOF exhibited distinct peaks at  $2\theta$  values of  $11.6^\circ$ ,  $13.5^\circ$ ,  $17.4^\circ$ ,  $19.04^\circ$ ,  $26.1^\circ$ ,  $29.5^\circ$ ,  $35.1^\circ$ , and  $39.2^\circ$ , corresponding to the crystal planes (222), (400), (333), (440), (553), (751), (951), and (882). These peaks were consistent with the crystal planes reported in the literature (JCPDS No. 00-065-1028).<sup>30</sup>

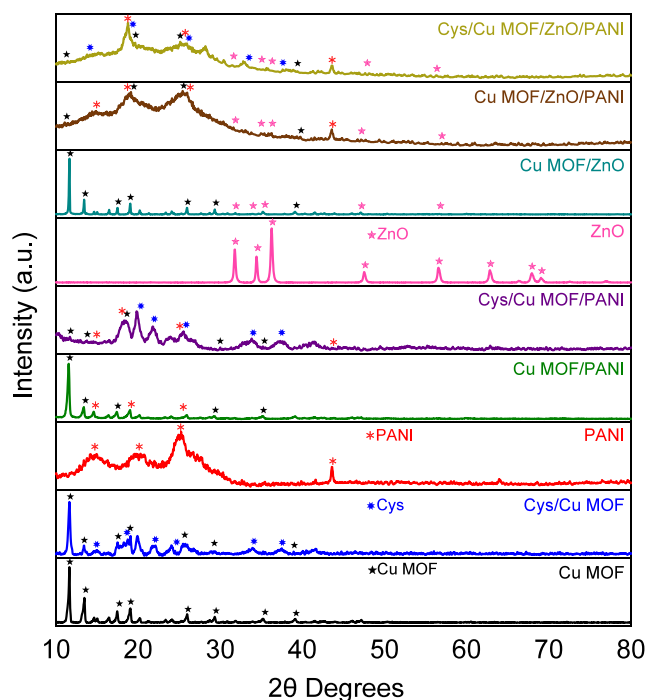


**Figure 2.** XRD Results of Cu MOF, Cys/Cu MOF composite, PANI nanotubes, Cu MOF/PANI composite, Cys/Cu MOF/PANI composite, ZnO NPs, Cu MOF/ZnO composite, Cu MOF/ZnO/PANI composite, and Cys/Cu MOF/ZnO/PANI nanocomposite.

The clearly defined sharp peaks imply a high degree of crystallinity in the structure. The XRD pattern of the functionalized Cu MOF reveals additional peaks associated with the cysteine at specific  $2\theta$  values of  $14.85^\circ$ ,  $19.0^\circ$ ,  $22.2^\circ$ ,  $25.4^\circ$ ,  $33.9^\circ$ , and  $37.5^\circ$ , which correspond to the crystallographic planes (20-2), (11-1), (401), (311), (800), and (512) crystal planes reported in the literature (JCPDS No. 00-056-1617).<sup>32</sup> These reflections confirm the functionalization of the Cu MOF. When comparing the diffraction peaks of the functionalized sample with the original Cu MOF, a certain degree of amorphous character could be observed. Also, a slight shift in the planes' degrees of the Bragg diffraction angle could be observed, which could be due to the pore-filling effect of the channel in the porous material. The XRD pattern of PANI exhibited distinct peaks at  $2\theta$  values of  $15.4^\circ$ ,  $19.05^\circ$ ,  $25.4^\circ$ , and  $45.1^\circ$  as reported in the literature (JCPDS No. 00-067-1544).<sup>41</sup> One can notice broad and diffuse humps in the material, which indicate the uneven distribution of interatomic distances. The XRD analysis of the Cu MOF/PANI composite showed diffraction peaks that matched those of the original MOF structure. Significantly, there were no identifiable diffraction peaks associated with PANI, most likely because the crystalline structure of the MOF was more prominent and overshadowed the distinctive features of PANI. This finding indicates that the degree of crystallinity of the MOF has a considerable impact on the structural characteristics of the composite, hence modifying the naturally noncrystalline structure of PANI.

Similarly, the XRD pattern of the Cys/Cu MOF/PANI composite exhibited distinct peaks, suggesting the presence of crystalline Cu MOF. The diffraction peaks exhibited decreased intensity, which can be attributed to the functionalization of the MOF with cysteine. The functionalization process also led to the displacement of certain crystallographic planes, which

may be associated with the filling of pores within the MOF structure. Furthermore, broad peaks specific to polyaniline were observed, confirming that its amorphous nature is still present in the composite. These observations emphasize the intricate relationship between the crystalline Cu MOF and the functionalized components, emphasizing the structural alterations caused by the inclusion of cysteine and polyaniline.

Also, the XRD analysis of ZnO NPs revealed distinct peaks at  $2\theta$  values =  $31.7^\circ$ ,  $34.4^\circ$ ,  $36.2^\circ$ ,  $47.5^\circ$ ,  $56.6^\circ$ ,  $62.8^\circ$ ,  $66.3^\circ$ ,  $69.1^\circ$ , and  $76.9^\circ$ . These peaks correspond to the crystal planes (100), (002), (101), (102), (110), (103), (200), (201), and (202) as reported in the literature (JCPDS No. 01-071-6424).<sup>42</sup> These peaks align with the established crystal planes of ZnO. The presence of well-defined and intense diffraction peaks in the ZnO indicates a highly crystalline structure, highlighting its remarkable sharpness and intensity. The XRD analysis of the Cu MOF/ZnO composite revealed well-defined peaks corresponding to the MOF component, indicating a significant level of crystallinity in the composite structure and a considerable particle size. The reduced magnitude of the ZnO peaks in the composite can be ascribed to the elevated concentration of the MOF. This observation indicates that the inclusion of the MOF in the composite has a considerable effect on the overall diffraction pattern, explicitly affecting the visibility of the distinctive peaks of ZnO. The XRD analysis of the Cu MOF/ZnO/PANI composite revealed a higher intensity at the  $19.04^\circ$  peak, which was absent in the pure PANI. The increased peak can be associated with overlapping diffraction peaks originating from the MOF and PANI constituents. Furthermore, a decrease in the intensity of the ZnO peaks was noted, confirming its incorporation into the composite matrix. The XRD results and the observed changes in the Cu MOF's shape validate the successful formation of the Cu MOF/ZnO/PANI composite. Each component plays a role in shaping and affecting the overall structure of the composite. The XRD analysis of the Cys/Cu MOF/ZnO/PANI nanocomposite revealed peaks at  $19.0^\circ$  and  $25.4^\circ$ , attributable to the overlapping diffraction peaks from the cysteine and PANI components.

**3.3. Fourier Transform Infrared Spectroscopy.** The FTIR spectra of all the produced samples were compared in the wavenumber range of  $4000\text{ cm}^{-1}$  to  $500\text{ cm}^{-1}$ , as shown in Figure 3. The spectra of Cu MOF exhibit a distinct vibration around  $724\text{ cm}^{-1}$ , attributed to the stretching of Cu–O bonds. This suggests that oxygen atoms are coordinating with Cu ions. The band noticed at a wavenumber of  $1425\text{ cm}^{-1}$  is associated with the vibrations of C–C bonds within the aromatic ring. Furthermore, the peak observed at  $1357\text{ cm}^{-1}$  corresponds to the stretching of C–O bonds in carboxylic acid functional groups.

The asymmetric stretching vibrations of the carboxylate groups produce the  $1636\text{ cm}^{-1}$  vibrational band in the MOF linker. However, this band may also arise via the benzene ring's elongation and the water molecules' vibrational distortion. Furthermore, a broad peak ranging from  $3100$  to  $3600\text{ cm}^{-1}$  suggests the presence of water molecules that are weakly bound to the Cu MOF complex. This peak arises from the stretching vibrations of OH groups in the water molecules.<sup>30,43</sup> The FTIR spectra of the Cysteine-grafted Cu MOF exhibited all the distinctive peaks of the parent Cu MOF, along with an additional prominent peak at  $3237\text{ cm}^{-1}$ . The presence of this peak can be associated with the stretching vibrational modes of the N–H group, providing evidence that the Cu MOF has

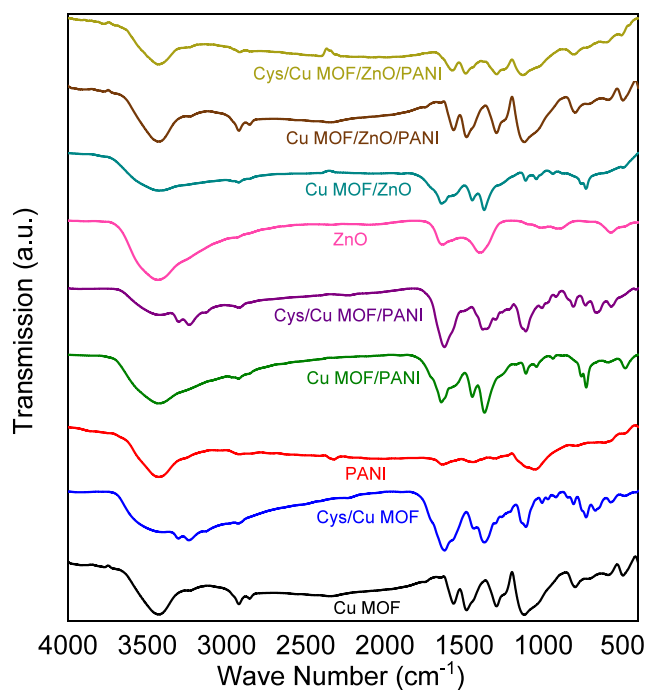


**Figure 3.** FTIR analysis of Cu MOF, Cys/Cu MOF composite, PANI nanotubes, Cu MOF/PANI composite, Cys/Cu MOF/PANI composite, ZnO NPs, Cu MOF/ZnO composite, Cu MOF/ZnO/PANI composite, and Cys/Cu MOF/ZnO/PANI nanocomposite.

been successfully functionalized with the cysteine. Furthermore, there is a distinct peak at  $573\text{ cm}^{-1}$ , which suggests the existence of S–S bond stretching vibrations. A distinctive vibrational band related to the S–H bond is observed at a frequency of  $2555\text{ cm}^{-1}$ . In addition, the presence of absorption peaks at  $1442\text{ cm}^{-1}$  in the cysteine grafted Cu MOF can be attributed to the stretching vibrations of the C–N bonds, which further confirms the incorporation of cysteine into the structure of the Cu MOF.<sup>32,44</sup>

In the case of PANI's FTIR spectra, the bending C–H peak of the aromatic ring, found at  $558\text{ cm}^{-1}$ , is a sign of the aromatic structure of the PANI. The C–H vibration in the para-coupled benzene and benzenoid rings is responsible for the peak at  $779\text{ cm}^{-1}$ . A peak resulting from the benzenoid ring's C–N stretching is seen at  $1053\text{ cm}^{-1}$ , emphasizing the nitrogen present in the PANI backbone. The peak further confirms the distinctive structure of PANI at  $1442\text{ cm}^{-1}$ , which is associated with the C=C stretching of the benzenoid ring. The quinonoid ring's C=C stretching peak, a key element of PANI's conductive qualities, is at  $1636\text{ cm}^{-1}$ . Lastly, the peak at  $3428\text{ cm}^{-1}$  is ascribed to secondary amines' N–H stretching vibration, which denotes the amine functional groups that are a part of PANI's molecular structure.<sup>45,46</sup>

In the case of Cu MOF/PANI composite, the peaks at  $1369$  and  $1449\text{ cm}^{-1}$  represent the C–N stretching of the aromatic ring and the C=C stretching of the benzenoid ring, respectively. Furthermore, the successful formation of the Cu MOF/PANI composite is further confirmed by the appearance of bands at  $1105$  and  $1645\text{ cm}^{-1}$ , which could be due to the C–O stretching of the primary alcohol and the asymmetric stretching vibration of the carboxylate group in the MOF linker, respectively.

Similarly, in the case of the Cys/Cu MOF/PANI composite, the carboxylate group's asymmetric and symmetric stretching

vibrations result in peaks at 1381 and 1623  $\text{cm}^{-1}$ , respectively. The OH stretching vibration at 3422  $\text{cm}^{-1}$  indicates the hydroxyl groups linked to the MOF. The C–N stretching vibration is attributed to a peak at 1111  $\text{cm}^{-1}$ , whereas a peak indicates the N–H stretching vibration at 3235  $\text{cm}^{-1}$ . The peak that represents the cysteine thiol group is weak and not very noticeable.

The dominant peak observed in FTIR spectra for ZnO is commonly located at a wavenumber of 573  $\text{cm}^{-1}$ . This peak is attributed to the stretching vibrations of the Zn–O bonds, an inherent feature of ZnO's crystal structure. The absorption peak at 3433  $\text{cm}^{-1}$  relates to the stretching of the O–H bond, whereas the peak at 1635  $\text{cm}^{-1}$  corresponds to the stretching of the C–C bond in an aromatic compound.<sup>42,47</sup> The FTIR spectra of Cu MOF/ZnO exhibit a significantly diminished peak at approximately 1700  $\text{cm}^{-1}$  and the emergence of two new peaks at 1642 and 1447  $\text{cm}^{-1}$ . This observation suggests the coordination of the carboxyl group with the Zn metal. When carboxylate groups bind with metal ions, they usually experience a decrease in the stretching frequency of the COOH group from around 1700  $\text{cm}^{-1}$  to the lower values. This change occurs because a metal-carboxylate connection is formed.

The creation of this bond impacts the electrical surroundings of the C=O and C–O bonds, resulting in a change in their vibrational frequencies. This is a prevalent process observed in MOF-metal oxide composites, wherein the functional groups in the MOF connect with the metal oxide particles, creating a composite material with modified characteristics.<sup>48</sup> The FTIR spectrum of the Cu MOF/ZnO/PANI ternary composite exhibits the distinct peaks associated with PANI. The vibration peaks around 496  $\text{cm}^{-1}$  confirmed the presence of Zn–O bonds, notably associated with ZnO. The peaks observed at 1295 and 1120  $\text{cm}^{-1}$  can be attributed to the stretching vibrations of the C–N bond in the benzenoid ring and the in-plane bending vibrations of the C–H bond, respectively. These peaks are indicative of the structural characteristics of PANI. Furthermore, a broad peak ranges from 3100 to 3600  $\text{cm}^{-1}$ , indicating water molecules loosely attached to the Cu MOF structure. The presence of separate spectral characteristics for each component in a single spectrum suggests the effective creation of the Cu MOF/ZnO/PANI ternary composite.<sup>49</sup> There are distinct peaks in the FTIR spectrum of the Cys/Cu MOF/ZnO/PANI nanocomposite that correspond to each component but with observable variations in peak positions. These shifts demonstrate the interactions between the components inside the nanocomposite structure. Moreover, the spectrum has a distinct 'laid down' appearance, marked by decreased peak intensities.

**3.4. Raman Spectroscopy.** Raman analysis confirmed the interaction between Cysteine, Cu MOF, ZnO, and PANI nanomaterials (Figure 4). During the Raman spectroscopy investigation of the Cu MOF, distinct vibrational bands are seen within the 1000 to 1520  $\text{cm}^{-1}$  frequency range. The bands correspond to the vibrational modes ( $\nu$ ) of the C=C bonds present in the benzene rings of the organic linker molecules. Moreover, the presence of bands at 710 and 810  $\text{cm}^{-1}$  suggests the occurrence of ring C–H bending vibrations. The detection of lower frequency bands aligns with the vibrations caused by stretching Cu–O bonds, supporting the findings previously documented in the literature. The spectrum evidence confirms the structural integrity and composition of the Cu MOF by identifying the specific vibrational fingerprints of its organic

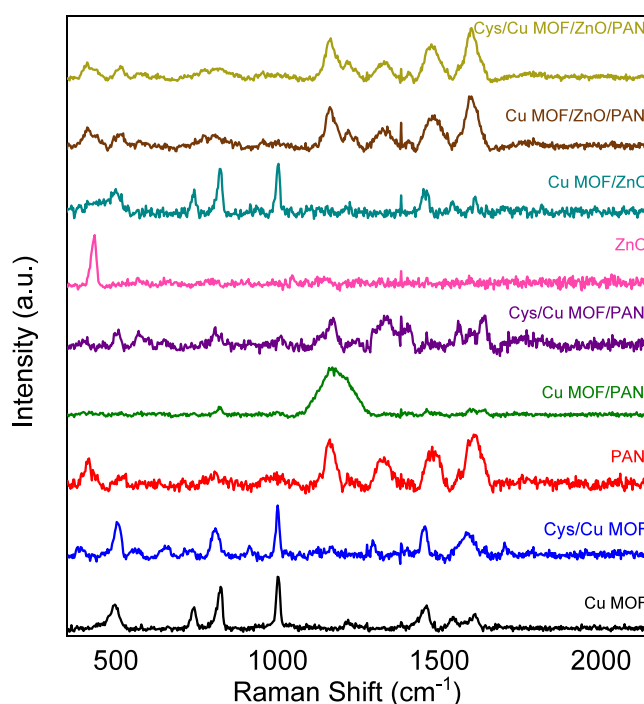


**Figure 4.** RAMAN spectra observed for Cu MOF, Cys/Cu MOF composite, PANI nanotubes, Cu MOF/PANI composite, Cys/Cu MOF/PANI composite, ZnO NPs, Cu MOF/ZnO nanocomposite, Cu MOF/ZnO/PANI nanocomposite, and Cys/Cu MOF/ZnO/PANI nanocomposite.

and inorganic components.<sup>39,50</sup> The Raman spectra of Cu MOF grafted with Cysteine exhibit all the characteristic peaks of Cu MOF and extra peaks corresponding to an amino acid. The S–H stretching vibrations exhibit significant Raman activity and produce a signal with great strength, making Raman spectroscopy the optimal method for observations. Additional vibrations related to sulfur are detected, such as an S–H bending mode at 941  $\text{cm}^{-1}$ , a cluster of C–S stretching modes at 616  $\text{cm}^{-1}$ , 660  $\text{cm}^{-1}$ , and 678  $\text{cm}^{-1}$ , and S–S stretching modes at 498  $\text{cm}^{-1}$ , 512  $\text{cm}^{-1}$ , and 529  $\text{cm}^{-1}$ .<sup>51</sup> The modes seen at 512 and 529  $\text{cm}^{-1}$  correspond to two distinct conformers of the disulfide bond, namely the gauche–gauche–gauche (GGG) and gauche–gauche–trans (GGT) conformers.<sup>52</sup> These modes are anticipated to undergo significant modifications when the Cys thiol is altered and can serve as a means to detect such alterations. Several other modes can be observed in the 250–1500  $\text{cm}^{-1}$  range, originating from different Cys vibrations. One example is the CH<sub>2</sub> rocking vibration at 775  $\text{cm}^{-1}$ , which has been extensively documented in other sources.<sup>53,54</sup>

An additional peak at 1158  $\text{cm}^{-1}$  in amino acid-modified Cu MOFs can be attributed to the N–H stretching vibrational mode, which confirms the successful modification of Cu MOF by amino acids.<sup>32,55</sup> The Raman spectra of PANI indicate the presence of an absorption band at 806  $\text{cm}^{-1}$ , which corresponds to the out-of-plane deformation bending of the C–H bonds in the benzene ring. The presence of the absorption band at 1138  $\text{cm}^{-1}$  can be attributed to the vibration mode of the N–H. The band observed at 1493  $\text{cm}^{-1}$  corresponds to the stretching vibration of the C=N bond, while the peak at 1575  $\text{cm}^{-1}$  is related to the stretching vibration of the C=C bond. These vibrations indicate the deformation of the benzenoid and quinoid rings.<sup>39,56</sup>

Similarly, the composite spectrum shows distinct bands at 665, 826, and 1164  $\text{cm}^{-1}$  corresponding to the bending of C–H bonds within the plane of the quinoid structure, stretching of the benzoic symmetry ring, and deformation of the semiquinoid ring. A distinct peak at 1394  $\text{cm}^{-1}$  can be attributed to the electrostatic interactions between the partially negative charge of the organic linker on the MOF and the partially positive nitrogen of PANI. Furthermore, the composite's peak corresponding to MOF changed from 605 to 665  $\text{cm}^{-1}$ . The apparent alterations indicated the presence of a correlation between MOF and PANI, as the transition metal Cu has a propensity to create coordination compounds with the nitrogen atom in PANI.<sup>57,58</sup>

The Raman spectra of ZnO NPs exhibit a prominent peak at 437  $\text{cm}^{-1}$ , corresponding to the E2 (high) mode. This peak indicates the wurtzite structure and is a reliable indicator of high-quality crystalline structure. The spectrum characteristics observed at 570 and 860  $\text{cm}^{-1}$  are associated with the specific vibrational modes of the Zn–O link, indicating the existence and creation of ZnO particles. The absorption peaks offer vital insights into the ZnO lattice's structural integrity and chemical connectivity.<sup>59,60</sup> The Raman spectra of the Cu MOF/ZnO exhibit distinct peaks that represent the structural characteristics of both components. Significantly, a Raman shift occurs, leading to two distinguishable peaks at around 450 and 577  $\text{cm}^{-1}$ . These peaks are ascribed to the A1 longitudinal optical (LO) mode and the E2 (high) mode of the ZnO wurtzite structure, respectively. These peaks indicate the high crystallinity of ZnO in composite, which is essential for applications that depend on the material's distinct optical and electrical characteristics.<sup>61</sup>

Similarly, the Cu MOF/ZnO/PANI nanocomposite signal observed at 437  $\text{cm}^{-1}$  corresponds to ZnO's E2 (high) mode, indicating its wurtzite structure. The peak shows conducting polymer chains at 1643  $\text{cm}^{-1}$ , which is associated with the C=C stretching vibrations in the quinoid structures of PANI. Furthermore, the presence of a peak shift in the Cu MOF provides evidence for the successful combination of these elements, indicating the formation of the composite. The Raman spectra of the Cys/Cu MOF/PANI/ZnO nanocomposite exhibit peak position shifts, which provide evidence for the presence of all constituent components and indicate their successful integration. These modifications imply interactions between the different elements, suggesting the possibility of a synergistic impact.

**3.5. Electrochemical Studies.** The modified GCE was subjected to electrochemical testing in a 0.1 M phosphate buffer saline (PBS) electrolytic solution with a pH of 7. 0.1 M PBS tablet was dissolved in 200 mL of deionized water. After the complete absorption of the solution, 0.2 mM of dopamine (3 mg in 100 mL) was added in the solution. Electrochemical investigations were performed with a three-electrode configuration, comprising a platinum wire as the counter electrode, an Ag/AgCl electrode as the reference electrode, and the working electrode was glassy carbon modified with each nanocomposite. The electrochemical experiments were conducted using a scan rate of 50  $\text{mVs}^{-1}$  within a potential range from  $-0.4$  to  $0.6$  V. This potential range is frequently used as it adequately includes both the oxidation and reduction peaks of electroactive species while avoiding excessive overpotentials that may compromise the integrity of the electrode material. It facilitates excellent electron transmission and offers an opportunity to examine the redox behavior of materials such

as Cu MOFs in a stable environment.<sup>62,63</sup> During the electrochemical process, dopamine (DA) is oxidized, converting the catechol group into *o*-quinone—the oxidation of DA results in the creation of dopamine *o*-quinone via a two-electron transfer mechanism. When dopamine undergoes oxidation, it releases electrons, which generate currents directly proportional to the concentration of electroactive dopamine biomolecules. Various electroanalytical techniques, such as cyclic voltammetry (CV) and chronoamperometry, can be employed to detect dopamine.

Figure 5 illustrates the cyclic voltammograms (CVs) of various electrode setups, including bare GCE, Cu MOF, Cys/

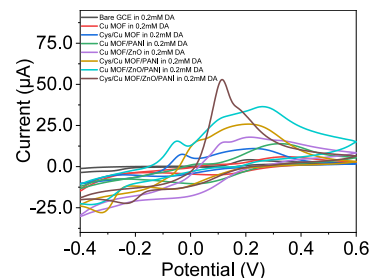


**Figure 5.** Cyclic voltammograms recorded in the presence of 0.2 mM dopamine (DA) and 0.1 M PBS electrolyte at a scan rate of 50  $\text{mVs}^{-1}$  for bare GCE, Cu MOF, Cys/Cu MOF, Cu MOF/PANI, Cu MOF/ZnO, Cys/Cu MOF/PANI, Cu MOF/ZnO/PANI, and Cys/Cu MOF/ZnO/PANI nanocomposite.

Cu MOF, Cu MOF/PANI, Cu MOF/ZnO, Cys/Cu MOF/PANI, Cu MOF/ZnO/PANI, Cys/Cu MOF/ZnO/PANI in the presence of 0.2 mM dopamine. The oxidation peak currents for the different nanocomposites were measured at specific potentials. The values observed for the bare GCE, Cu MOF, Cys/Cu MOF, Cu MOF/PANI, Cu MOF/ZnO, Cys/Cu MOF/PANI, Cu MOF/ZnO/PANI nanocomposites were 5.9  $\mu\text{A}$ , 10.9  $\mu\text{A}$ , 13.9  $\mu\text{A}$ , 17.9  $\mu\text{A}$ , 25.8  $\mu\text{A}$ , 36.4  $\mu\text{A}$ , and 52.4  $\mu\text{A}$ , respectively. These measurements were taken at potentials of 0.344, 0.229, 0.324, 0.215, 0.210, 0.260, and 0.114 V. For comparison, CV graphs for each material on modified GCE are presented in Figure S1. The peak current values indicate that the Cu MOF-modified electrode has a considerably higher peak current than the bare GCE. This is likely due to its large surface area, distinctive porous structure, and enhanced adsorption capability, allowing for a more excellent DA collection on the modified electrode surface. The addition of cysteine in Cys/Cu MOF results in a more significant peak current. This is because cysteine has a thiol group that forms bonds with metals, enhancing the sensitivity and selectivity of the electrode. Incorporating PANI into Cu MOF/PANI and Cys/Cu MOF/PANI composites further enhances oxidation peak currents. PANI's conductive character enhances the electrode's active sites by promoting ions' passage and electrons' transport in redox reactions. Furthermore, adding ZnO in Cu MOF/ZnO and its resulting composites enhances peak current. This is due to the advantageous properties of ZnO, such as its high electron mobility, stability, biocompatibility, and nanostructured morphology. These properties increase electrode surface area, improving sensitivity and reaction kinetics. The Cys/Cu MOF/ZnO/PANI nanocomposite exhibits a remarkably elevated peak current, suggesting a substantial enhancement in the electron transfer reaction. This enhancement is most likely attributed to the

synergistic effects resulting from the combination of ZnO nanoparticles and PANI. These nanoparticles enhance the catalytic activity of the electrode toward dopamine oxidation because of their tiny size and large surface area. The combined effect of the conductive nanomaterials (ZnO and PANI) and the functional properties of cysteine and Cu MOF results in a highly efficient catalytic performance and a higher current density of the redox peak. This demonstrates a significant improvement compared to the individual material components.

Dopamine typically experiences a two-electron, two-proton oxidation reaction, resulting in the formation of dopamine quinone. Under standard conditions, this oxidation process occurs rapidly and typically yields a single, clearly defined anodic peak. Nonetheless, the interaction between dopamine and the electrode is transformed when the electrode surface is altered with materials such as Cu MOFs, Cys/Cu MOFs, PANI, and ZnO. These compositions can affect the electrochemical environment, introducing supplementary redox processes that provide multiple anodic peaks or irregularities. The factors contributing to these supplementary peaks could be due to modified surfaces which can enhance or modify electron transport kinetics. For instance, Cu MOFs may generate distinct active sites or routes for dopamine oxidation, leading to peaks at varying potentials. The interaction of dopamine with these complex surfaces may result in intermediate oxidation states or numerous phases in the oxidation process, exhibiting more than one peak. Also, the altered electrode surfaces may influence the adsorption of dopamine or its oxidation products, resulting in supplementary peaks. Adsorbed species can generate novel oxidation and reduction peaks due to their distinct interactions with the electrode material.

The Cys/Cu MOF/ZnO/PANI modified GCE CV curves at various scan rates are displayed in Figure 6, along with the

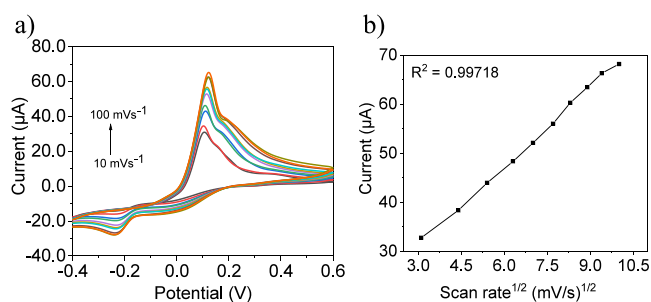


**Figure 6.** (a) Cyclic voltammograms recorded for Cys/Cu MOF/ZnO/PANI in the presence of 0.2 mM dopamine (DA) and 0.1 M PBS electrolyte at different scan rates from 10–100  $\text{mVs}^{-1}$ . (b) Corresponding plot of oxidation peak current ( $I_{pa}$ ) against the square root of the scan rate.

linear relationship between the anodic and cathodic peak currents and the square root of the scan rates. Figure 6a shows that the anodic and cathodic peak currents for the Cys/Cu MOF/ZnO/PANI modified electrode increased with the increased potential scan rate (10 to 100  $\text{mVs}^{-1}$ ). The faster scan rates caused the diffusion layer size to decrease, leading to higher currents. The square root of the scan rates is plotted between the anodic peak currents in Figure 6b, revealing a linear relationship with a correlation coefficient value of

0.99718 for the anodic peak, respectively, indicating that the oxidation process is diffusion-controlled.

The Cys/Cu MOF/ZnO/PANI CV curves show the anodic peak currents increased linearly with the increase in DA concentration, as measured in 0.1 M PBS with a modified electrode for DA concentrations ranging from 0.05 mM to 0.8 mM (Figure 7). This suggests that the Cys/Cu MOF/ZnO/PANI has excellent catalytic activity for the electro-oxidation of DA.

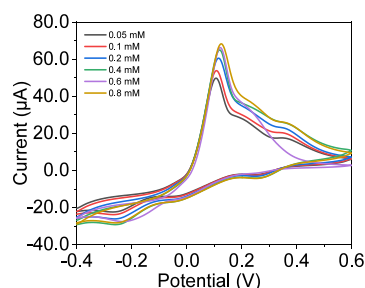


**Figure 7.** Cyclic voltammogram of Cys/Cu MOF/ZnO/PANI modified GCE in the presence of different concentrations of dopamine (DA) at a scan rate of 50  $\text{mVs}^{-1}$ .

**3.6. Detection of Dopamine through Differential Pulse Voltammetry (DPV).** DPV was used to quantify various concentrations of DA on GCE modified with Cys/Cu MOF/ZnO/PANI under the most suitable experimental conditions. We used DPV to quantify dopamine because it provides a distinct oxidation peak at a specific potential, allowing clear molecule identification. DPV is ideal for this, as the peak corresponds directly to dopamine's redox reaction. The scanning potential window ranged from  $-0.1$  to  $0.3$  V (Figure 8). Figure 8a shows that increasing the dopamine

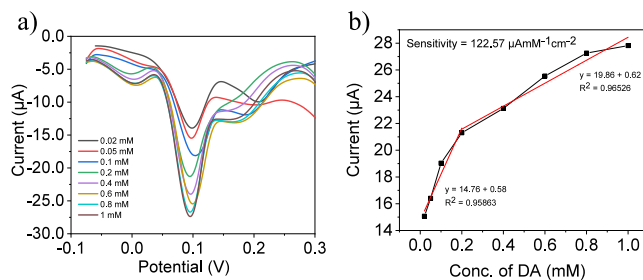


**Figure 8.** (a) DPV curves of different concentrations of DA, i.e., 0.02 mM to 1 mM in 0.1 M PBS on Cys/Cu MOF/ZnO/PANI in the range of  $-0.1$  to  $3.0$  V at a scan rate of 50  $\text{mVs}^{-1}$ . (b) Corresponding linear calibration curve of peak current vs DA concentration.

concentration from 0.02 mM to 1 mM elevated  $I_{pc}$ . The calibration curve in Figure 8b demonstrates that as the dopamine concentration is increased to higher values, there is a corresponding increase in the current response. At more significant dopamine concentrations, the dopamine molecules are absorbed onto the surface of the electrode, covering all the active sites. The sensor achieved a sensitivity of  $122.57 \mu\text{AmM}^{-1} \text{cm}^{-2}$  and a detection limit of  $0.39 \mu\text{M}$ . These values are also compared with the other nanocomposites in Table 1.

**3.7. Influence of Solution pH.** The pH of the solution significantly influences the electrical signal response of dopamine due to protons participating in the electrooxidation process.<sup>75,76</sup> Consequently, the impact of different pH levels

**Table 1. Comparison of Different Sensitivity Values of Dopamine Sensors**

electrode materials	LOD ( $\mu\text{M}$ )	sensitivity ( $\mu\text{AmM}^{-1}\text{cm}^{-2}$ )	reference
CHCF-FMF	13	100.64	64
Zn-MOF-U	0.003	15.6	65
CuO/Cu <sub>2</sub> O	0.388	0.00922	66
PANI/ITm:ZnO	1.92	0.0002568	67
LaFeO <sub>3</sub> NPs@CNTs	0.05	0.005980	68
In <sub>2</sub> O <sub>3</sub> :ZnO@MC	0.024	0.0002153	69
g-C <sub>3</sub> N <sub>4</sub> /GO	0.0054		70
G-SnO <sub>2</sub>	1		71
Fe <sub>2</sub> O <sub>3</sub> /N-rGO	0.49	418.6	72
GO/WO <sub>3</sub>	0.306	392	73
PPy-MCM-48/Au	0.70		74
Cysteine Grafted Cu MOF/ ZnO/PANI	0.39	122.57	this work

(1.0–11.0) was examined utilizing the Cys/Cu MOF/ZnO/PANI modified GCE for 0.2 mM DA in 0.1 M PBS at a scan rate of 50 mVs<sup>-1</sup> (Figure 9). The anodic peak current of DA

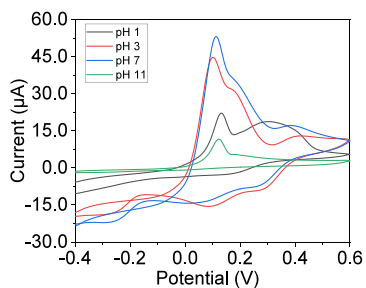


**Figure 9.** Cys/Cu MOF/ZnO/PANI modified GCE was tested with CVs of 0.2 mM DA in 0.1 M PBS at different pHs (1.0, 3.0, 7.0, and 11.0) at a scan rate of 50 mVs<sup>-1</sup>.

increased with pH rising from 1.0 to 7.0, then declined at pH 11.0. The peak sensitivity is noted at pH 7.0, attributed to full deprotonation, making it potentially acceptable for biological applications. Consequently, a pH of 7.0 is the most suitable value for subsequent investigations.

**3.8. Reproducibility, Repeatability, and Stability of the Cys/Cu MOF/ZnO/PANI Modified GCE.** The reproducibility, repeatability, and stability of the Cys/Cu MOF/ZnO/PANI modified GCE for DA determination were examined, as illustrated in Figure 10. The repeatability of the modified electrode was assessed through sequential measurements of 11 0.1 M PBS (pH 7.0) solutions containing 0.2 mM DA, resulting in a relative standard deviation of 2.91%, as illustrated in Figure 10a. Subsequently, Figure 10b illustrates the reproducibility of the produced sensor, achieved by producing four independently modified Cys/Cu MOF/ZnO/PANI GCEs under identical conditions, used to detect 0.2 mM DA in 0.1 M PBS at pH 7.0 (RSD is 1.23%). Furthermore, the stability of the fabricated sensor was assessed in 0.1 M PBS at ambient temperature. For 2 weeks, no notable change in the oxidation peak potential of DA was observed, accompanied by a 4.07% decrease in current, as illustrated in Figure 10c. Consequently, all these findings suggest that the Cys/Cu MOF/ZnO/PANI modified GCE has excellent reproducibility, repeatability, and stability.

**3.9. Selectivity Study.** To assess the selectivity of the Cys/Cu MOF/ZnO/PANI nanocomposite-modified GCE toward DA, chronoamperometric measurements were conducted at a particular applied potential. While it monitors current changes over time, it does not provide the specific redox potentials needed for molecular qualification. Therefore, DPV was used for dopamine qualification, and it was used to assess sensor selectivity under constant potential conditions. The voltage measured is 0.25 V in a 0.1 M PBS solution despite common biological interferences such as glucose (Glu), ascorbic acid (AA), and urea. It is evident that the

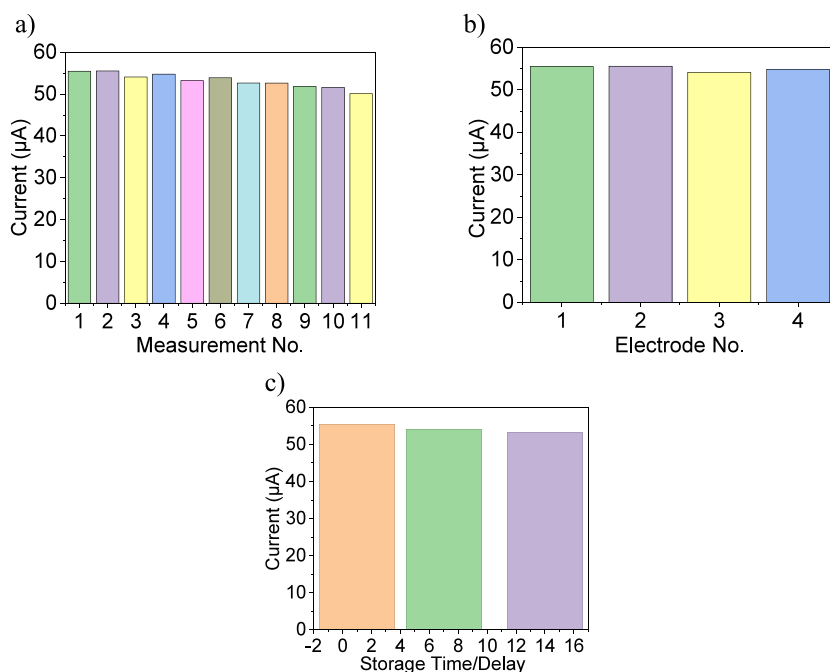


**Figure 10.** Measurements of the anodic peak current of 0.8 mM DA in 0.1 M PBS (pH 7.0) at a scan rate of 50 mVs<sup>-1</sup> were conducted for (a) 11 instances at the Cys/Cu MOF/ZnO/PANI modified GCE, (b) four distinct electrodes, and (c) different storage periods.

current value significantly increases when 0.2 mM DA is added (Figure 11). However, when other interfering biological

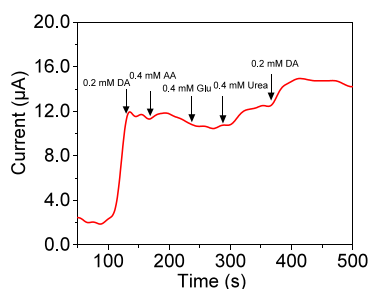


**Figure 11.** Chronoamperometric curve was gathered for a modified Cys/Cu MOF/ZnO/PANI electrode. The curve was generated by adding dopamine (DA) and common interferences, ascorbic acid, glucose, and urea, with a voltage of 0.25 V.

chemicals are introduced, even at a hundred times greater concentrations, there is no apparent change in the current value. Additionally, the addition of the DA increases current, providing further evidence that the manufactured Cys/Cu MOF/ZnO/PANI modified electrode exhibits more excellent selectivity toward DA.

#### 4. CONCLUSIONS

This study presents a novel electrochemical sensor based on Cys/Cu MOF/ZnO/PANI nanocomposite for detecting dopamine. The primary objective of this study was to showcase the combined impact of Cys/Cu MOF/ZnO/PANI in the advancement of a dopamine sensor. The electrode we created has a high sensitivity of  $122.57 \mu\text{AmM}^{-1} \text{cm}^{-2}$  and can selectively detect dopamine within a detection limit of  $0.39 \mu\text{M}$ . Furthermore, the electrochemical sensor exhibited remarkable selectivity for dopamine, even when glucose, urea, and ascorbic acid were present. The electrochemical investigations indicate that the GEC modified with the investigated nanocomposite, Cysteine grafted Cu MOF/ZnO/PANI, exhibits significant promise as an electrochemical sensor for detecting Dopamine.

#### ■ ASSOCIATED CONTENT

##### Data Availability Statement

All the relevant data supporting this article have been included in the manuscript.

##### Supporting Information

The Supporting Information is available free of charge at <https://pubs.acs.org/doi/10.1021/acsomega.4c07452>.

Individual CV graph for each material on modified GCE (PDF)

#### ■ AUTHOR INFORMATION

##### Corresponding Author

Zakir Hussain – School of Chemical and Materials Engineering (SCME), National University of Sciences and Technology (NUST), Islamabad 44000, Pakistan;  
 orcid.org/0000-0003-4850-362X; Email: zakir.hussain@scme.nust.edu.pk

##### Authors

Mariam Basharat – School of Chemical and Materials Engineering (SCME), National University of Sciences and

Technology (NUST), Islamabad 44000, Pakistan;

orcid.org/0009-0007-5336-1722

Dooa Arif – School of Chemical and Materials Engineering (SCME), National University of Sciences and Technology (NUST), Islamabad 44000, Pakistan

Waheed Miran – School of Chemical and Materials Engineering (SCME), National University of Sciences and Technology (NUST), Islamabad 44000, Pakistan

Complete contact information is available at:

<https://pubs.acs.org/10.1021/acsomega.4c07452>

#### Author Contributions

M.B.: methodology, writing—original draft, investigation, and characterization. D.A.: review and editing and characterization. Z.H.: conceptualization, supervision, and reviewing of manuscript. W.M.: characterization and reviewing of manuscript.

#### Funding

No external funding was involved in the present research.

#### Notes

The authors declare no competing financial interest.

#### ■ ACKNOWLEDGMENTS

This research was conducted at the School of Chemical and Materials Engineering (SCME), National University of Sciences and Technology, Sector H-12, Islamabad. Z.H. acknowledges the financial and administrative support from the SCME.

#### ■ REFERENCES

- Carlsson, A. Perspectives on the discovery of central monoaminergic neurotransmission. *Annu. Rev. Neurosci.* **1987**, *10* (1), 19–40.
- Reis, H. J.; Guatimosim, C.; Paquet, M.; Santos, M.; Ribeiro, F. M.; Kummer, A.; Schenatto, G.; Salgado, J. V.; Vieira, L. B.; Teixeira, A. L. Neuro-transmitters in the central nervous system & their implication in learning and memory processes. *Curr. Med. Chem.* **2009**, *16* (7), 796–840.
- Mehler-Wex, C.; Riederer, P.; Gerlach, M. Dopaminergic dysbalance in distinct basal ganglia neurocircuits: implications for the pathophysiology of Parkinson's disease, schizophrenia and attention deficit hyperactivity disorder. *Neurotox. Res.* **2006**, *10*, 167–179.
- Wei, N.; Zhao, X.-E.; Zhu, S.; He, Y.; Zheng, L.; Chen, G.; You, J.; Liu, S.; Liu, Z. Determination of dopamine, serotonin, biosynthesis precursors and metabolites in rat brain microdialysates by ultrasonically assisted in situ derivatization–dispersive liquid–liquid microextraction coupled with UHPLC-MS/MS. *Talanta* **2016**, *161*, 253–264.
- Dutta, G.; Tan, C.; Siddiqui, S.; Arumugam, P. U. Enabling long term monitoring of dopamine using dimensionally stable ultranocrystalline diamond microelectrodes. *Mater. Res. Exp.* **2016**, *3* (9), No. 094001.
- Shao, Y.; Wang, J.; Wu, H.; Liu, J.; Aksay, I. A.; Lin, Y. Graphene based electrochemical sensors and biosensors: a review. *Electroanal.* **2010**, *22* (10), 1027–1036.
- Wang, T.; Xia, Y.; Wan, X.; Zhang, Y.; Chen, N.; Jin, Y.; Li, G. A facile and efficient voltammetric sensor for marbofloxacin detection based on zirconium-based metal-organic framework UiO-66/nitrogen-doped graphene nanocomposite. *Microchem. J.* **2024**, *201*, No. 110673.
- Marlar, T.; Harb, J. N. MOF-Enabled Electrochemical Sensor for Rapid and Robust Sensing of V-Series Nerve Agents at Low Concentrations. *ACS Appl. Mater. & Inter.* **2024**, *16* (7), 9569–9580.
- Wan, X.; Du, H.; Tuo, D.; Qi, X.; Wang, T.; Wu, J.; Li, G. UiO-66/carboxylated multiwalled carbon nanotube composites for highly

- efficient and stable voltammetric sensors for gatifloxacin. *ACS Appl. Nano Mater.* **2023**, *6* (20), 19403–19413.
- (10) Nisar, A.; Khan, M. A.; Hussain, Z. Synthesis and characterization of PANI/MOF-199/Ag nanocomposite and its potential application as non-enzymatic electrochemical sensing of dopamine. *J. Kor. Cer. Soc.* **2022**, *59* (3), 359–369.
- (11) Ma, T.; Li, H.; Ma, J.-G.; Cheng, P. Application of MOF-based materials in electrochemical sensing. *Dal. Trans.* **2020**, *49* (47), 17121–17129.
- (12) Yang, H.; Liu, J.; Feng, X.; Nie, F.; Yang, G. A novel copper-based metal-organic framework as a peroxidase-mimicking enzyme and its glucose chemiluminescence sensing application. *Anal. Bioanal. Chem.* **2021**, *413* (17), 4407–4416.
- (13) Anuma, S.; Mishra, P.; Bhat, B. R. Polypyrrole functionalized Cobalt oxide Graphene (COPYGO) nanocomposite for the efficient removal of dyes and heavy metal pollutants from aqueous effluents. *J. Hazard. Mater.* **2021**, *416*, No. 125929.
- (14) GunaVathana, S. D.; Wilson, J.; Prashanthi, R.; Peter, A. C. CuO nanoflakes anchored polythiophene nanocomposite: Voltammetric detection of L-Tryptophan. *Inorg. Chem. Commun.* **2021**, *124*, No. 108398.
- (15) Wang, T.; Wang, Y.; Zhang, D.; Hu, X.; Zhang, L.; Zhao, C.; He, Y.-S.; Zhang, W.; Yang, N.; Ma, Z.-F. Structural tuning of a flexible and porous polypyrrole film by a template-assisted method for enhanced capacitance for supercapacitor applications. *ACS Appl. Mater. & Inter.* **2021**, *13* (15), 17726–17735.
- (16) Youssef, A. M.; Hasanin, M. S.; El-Aziz, M. E. A.; Turky, G. M. Conducting chitosan/hydroxyethyl cellulose/polyaniline bionanocomposites hydrogel based on graphene oxide doped with Ag-NPs. *Int. J. Biol. Macromol.* **2021**, *167*, 1435–1444.
- (17) Gao, F.; Luo, Y.; Xu, J.; Du, X.; Wang, H.; Cheng, X.; Du, Z. Preparation of graphene oxide-based polyaniline composites with synergistic anticorrosion effect for waterborne polyurethane anticorrosive coatings. *Prog. Org. Coat.* **2021**, *156*, No. 106233.
- (18) Liu, A.; Lv, S.; Jiang, L.; Liu, F.; Zhao, L.; Wang, J.; Hu, X.; Yang, Z.; He, J.; Wang, C.; Yan, X.; Sun, P.; Shimanoe, K.; Lu, G. The gas sensor utilizing polyaniline/MoS<sub>2</sub> nanosheets/SnO<sub>2</sub> nanotubes for the room temperature detection of ammonia. *Sens. Actuators, B* **2021**, *332*, No. 129444.
- (19) Wang, H.; Lin, J.; Shen, Z. X. Polyaniline (PANI) based electrode materials for energy storage and conversion. *J. Sc.: Adv. Mater. Dev.* **2016**, *1* (3), 225–255.
- (20) Yang, Y.; Heeger, A. Polyaniline as a transparent electrode for polymer light-emitting diodes: Lower operating voltage and higher efficiency. *Appl. Phys. Lett.* **1994**, *64* (10), 1245–1247.
- (21) Fazio, E.; Spadaro, S.; Corsaro, C.; Neri, G.; Leonardi, S. G.; Neri, F.; Lavanya, N.; Sekar, C.; Donato, N.; Neri, G. Metal-oxide based nanomaterials: Synthesis, characterization and their applications in electrical and electrochemical sensors. *Sensors* **2021**, *21* (7), 2494.
- (22) Maduraiveeran, G.; Jin, W. Nanomaterials based electrochemical sensor and biosensor platforms for environmental applications. *Trends in Env. Anal. Chem.* **2017**, *13*, 10–23.
- (23) Balkourani, G.; Damartzis, T.; Brouzgou, A.; Tsiakaras, P. Cost effective synthesis of graphene nanomaterials for non-enzymatic electrochemical sensors for glucose: a comprehensive review. *Sensors* **2022**, *22* (1), 355.
- (24) Lee, S.-H.; Galstyan, V.; Ponzoni, A.; Gonzalo-Juan, I.; Riedel, R.; Dourges, M.-A.; Nicolas, Y.; Toupance, T. Finely tuned SnO<sub>2</sub> nanoparticles for efficient detection of reducing and oxidizing gases: the influence of alkali metal cation on gas-sensing properties. *ACS Appl. Mater. & Inter.* **2018**, *10* (12), 10173–10184.
- (25) Beitollahi, H.; Tajik, S.; Nejad, F. G.; Safaei, M. Recent advances in ZnO nanostructure-based electrochemical sensors and biosensors. *J. Mater. Chem. B* **2020**, *8* (27), 5826–5844.
- (26) Sharma, N.; Ojha, H.; Bharadwaj, A.; Pathak, D. P.; Sharma, R. K. Preparation and catalytic applications of nanomaterials: a review. *RSC Adv.* **2015**, *5* (66), 53381–53403.
- (27) Polo-Garzon, F.; Bao, Z.; Zhang, X.; Huang, W.; Wu, Z. Surface reconstructions of metal oxides and the consequences on catalytic chemistry. *ACS Catal.* **2019**, *9* (6), 5692–5707.
- (28) Gellé, A.; Moores, A. Plasmonic nanoparticles: Photocatalysts with a bright future. *Current Opinion in Green and Sust. Chem.* **2019**, *15*, 60–66.
- (29) He, D.; Li, S.; Zhang, P.; Luo, H. CVD graphene incorporating polymerized l-cysteine as an electrochemical sensing platform for simultaneous determination of dopamine and ascorbic acid. *Anal. Meth.* **2017**, *9* (47), 6689–6697.
- (30) Lin, S.; Song, Z.; Che, G.; Ren, A.; Li, P.; Liu, C.; Zhang, J. Adsorption behavior of metal–organic frameworks for methylene blue from aqueous solution. *Microp. Mesop. Mater.* **2014**, *193*, 27–34.
- (31) Al-Janabi, N.; Deng, H.; Borges, J.; Liu, X.; Garforth, A.; Siperstein, F. R.; Fan, X. A facile post-synthetic modification method to improve hydrothermal stability and CO<sub>2</sub> selectivity of CuBTC metal–organic framework. *Ind. Eng. Chem. Res.* **2016**, *55* (29), 7941–7949.
- (32) Rani, R.; Deep, A.; Mizaikoff, B.; Singh, S. Enhanced hydrothermal stability of Cu MOF by post synthetic modification with amino acids. *Vacuum* **2019**, *164*, 449–457.
- (33) Fayemi, O. E.; Adekunle, A. S.; Swamy, B. K.; Ebenso, E. E. Electrochemical sensor for the detection of dopamine in real samples using polyaniline/NiO, ZnO, and Fe<sub>3</sub>O<sub>4</sub> nanocomposites on glassy carbon electrode. *J. Electroanal. Chem.* **2018**, *818*, 236–249.
- (34) Vinodh, R.; Babu, R. S.; Sambasivam, S.; Gopi, C. V. M.; Alzahmi, S.; Kim, H.-J.; de Barros, A. L. F.; Obaidat, I. M. Recent advancements of polyaniline/metal organic framework (PANI/MOF) composite electrodes for supercapacitor applications: a critical review. *Nanomater.* **2022**, *12* (9), 1511.
- (35) Gamedze, N. P.; Mthiyane, D. M.; Mavengahama, S.; Singh, M.; Onwudiwe, D. C. Biosynthesis of ZnO nanoparticles using the aqueous extract of *Mucuna pruriens* (utilis): structural characterization, and the anticancer and antioxidant activities. *Chem. Africa* **2024**, *7* (1), 219–228.
- (36) Bodkhe, G. A.; Kharat, H. J.; Kshirsagar, D. V.; Hedau, B. S.; Deshmukh, M. A.; Patil, H. K.; Shirsat, S. M.; Phase, D. M.; Shirsat, M. D. Polyaniline/ CuBTC metal organic framework composite for detection of ammonia. *Vidyabharati Int. Interdiscip. Res. J.* **2020**, *5*, 516–520.
- (37) Wang, Q. M.; Shen, D.; Bülow, M.; Lau, M. L.; Deng, S.; Fitch, F. R.; Lemcoff, N. O.; Semanscin, J. Metallo-organic molecular sieve for gas separation and purification. *Microporous Mesoporous Mater.* **2002**, *55* (2), 217–230.
- (38) Martina, V.; De Riccardis, M.; Carbone, D.; Rotolo, P.; Bozzini, B.; Mele, C. Electrodeposition of polyaniline–carbon nanotubes composite films and investigation on their role in corrosion protection of austenitic stainless steel by SNIFTIR analysis. *J. Nanopar. Res.* **2011**, *13*, 6035–6047.
- (39) Ramohlola, K. E.; Monana, G. R.; Hato, M. J.; Modibane, K. D.; Molapo, K. M.; Masikini, M.; Mduli, S. B.; Iwuoha, E. I. Polyaniline-metal organic framework nanocomposite as an efficient electrocatalyst for hydrogen evolution reaction. *Comp. Part B: Eng.* **2018**, *137*, 129–139.
- (40) Wojnarowicz, J.; Opalinska, A.; Chudoba, T.; Gierlotka, S.; Mukhovskiy, R.; Pietrzykowska, E.; Sobczak, K.; Lojkowski, W. Effect of water content in ethylene glycol solvent on the size of ZnO nanoparticles prepared using microwave solvothermal synthesis. *J. Nanomater.* **2016**, *2016*, 578.
- (41) Bhadra, S.; Khashtgir, D. Determination of crystal structure of polyaniline and substituted polyanilines through powder X-ray diffraction analysis. *Polym. Test.* **2008**, *27* (7), 851–857.
- (42) Kalpana, V. N.; Kataru, B. A. S.; Sravani, N.; Vigneshwari, T.; Panneerselvam, A.; Devi Rajeswari, V. Biosynthesis of zinc oxide nanoparticles using culture filtrates of *Aspergillus niger*: Antimicrobial textiles and dye degradation studies. *Open Nano* **2018**, *3*, 48–55.
- (43) Homayoonnia, S.; Zeinali, S. Design and fabrication of capacitive nanosensor based on MOF nanoparticles as sensing layer for VOCs detection. *Sens. Actuatur. B: Chem.* **2016**, *237*, 776–786.

- (44) Wei, S.; Guo, C.; Wang, L.; Xu, J.; Dong, H. Bacterial synthesis of PbS nanocrystallites in one-step with l-cysteine serving as both sulfur source and capping ligand. *Sci. Rep.* **2021**, *11* (1), 1216.
- (45) Ajeel, K. I.; Kareem, Q. S. Synthesis and characteristics of polyaniline (PANI) filled by graphene (PANI/GR) nano-films. *J. Phys.: Conf. Ser.* **2019**, No. 012020.
- (46) Ibrahim, K. A. Synthesis and characterization of polyaniline and poly (aniline-co-o-nitroaniline) using vibrational spectroscopy. *Arab. J. Chem.* **2017**, *10*, S2668–S2674.
- (47) Srivastava, V.; Choubey, A. K. Kinetic and isothermal study of effect of transition metal doping on adsorptive property of zinc oxide nanoparticles synthesized via green route using *Moringa oleifera* leaf extract. *Mater. Res. Exp.* **2019**, *6* (12), 1250i7.
- (48) Rahimi, R.; Shariatnia, S.; Zargari, S.; Berijani, M. Y.; Ghaffarinejad, A.; Shojaie, Z. S. Synthesis, characterization, and photocurrent generation of a new nanocomposite based Cu–TCPP MOF and ZnO nanorod. *RSC Adv.* **2015**, *5* (58), 46624–46631.
- (49) Zhu, C.; He, Y.; Liu, Y.; Kazantseva, N.; Saha, P.; Cheng, Q. ZnO@MOF@PANI core-shell nanoarrays on carbon cloth for high-performance supercapacitor electrodes. *J. Ener.Chem.* **2019**, *35*, 124–131.
- (50) Prestipino, C.; Regli, L.; Vitillo, J. G.; Bonino, F.; Damin, A.; Lamberti, C.; Zecchina, A.; Solari, P.; Kongshaug, K.; Bordiga, S. Local structure of framework Cu (II) in HKUST-1 metallorganic framework: spectroscopic characterization upon activation and interaction with adsorbates. *Chem. Mater.* **2006**, *18* (5), 1337–1346.
- (51) Bazylewski, P.; Divigalpitiya, R.; Fanchini, G. In situ Raman spectroscopy distinguishes between reversible and irreversible thiol modifications in l-cysteine. *RSC Adv.* **2017**, *7* (5), 2964–2970.
- (52) Van Wart, H. E.; Scheraga, H. A. Agreement with the disulfide stretching frequency-conformation correlation of Sugeta, Go, and Miyazawa. *Proc. Natl. Acad. Sci. U. S. A.* **1986**, *83* (10), 3064–3067.
- (53) Minkov, V. S.; Goryainov, S. V.; Boldyreva, E. V.; Görbitz, C. H. Raman study of pressure-induced phase transitions in crystals of orthorhombic and monoclinic polymorphs of l-cysteine: dynamics of the side chain. *J. Raman Spectrosc.* **2010**, *41* (12), 1748–1758.
- (54) Pawlukojć, A.; Leciejewicz, J.; Ramirez-Cuesta, A.; Nowicka-Scheibe, J. L-Cysteine: Neutron spectroscopy, Raman, IR and ab initio study. *Spectrochim. Acta Part A: Mol. Biomol. Spect.* **2005**, *61* (11–12), 2474–2481.
- (55) Zhu, G.; Zhu, X.; Fan, Q.; Wan, X. Raman spectra of amino acids and their aqueous solutions. *Spectrochim. Acta Part A: Mol. Biomol. Spect.* **2011**, *78* (3), 1187–1195.
- (56) Shao, W.; Jamal, R.; Xu, F.; Ubul, A.; Abdiryim, T. The effect of a small amount of water on the structure and electrochemical properties of solid-state synthesized polyaniline. *Materials* **2012**, *5* (10), 1811–1825.
- (57) Li, D.; Kaner, R. B. Processable stabilizer-free polyaniline nanofiber aqueous colloids. *Chem. Commun.* **2005**, *26*, 3286–3288.
- (58) Tao, S.; Hong, B.; Kerong, Z. An infrared and Raman spectroscopic study of polyanilines co-doped with metal ions and H<sup>+</sup>. *Spectrochim. Acta Part A: Mol. Biomol. Spect.* **2007**, *66* (4–5), 1364–1368.
- (59) da Trindade, L. G.; Borba, K. M.; Trench, A. B.; Zanchet, L.; Teodoro, V.; Pontes, F. M.; Longo, E.; Mazzo, T. M. Effective strategy to coupling Zr-MOF/ZnO: Synthesis, morphology and photo-electrochemical properties evaluation. *J. Solid State Chem.* **2021**, *293*, No. 121794.
- (60) Dev, S. S. G.; Sharma, V.; Singh, A.; Baghel, V. S.; Yanagida, M.; Nagataki, A.; Tripathi, N. Raman spectroscopic study of ZnO/NiO nanocomposites based on spatial correlation model. *RSC Adv.* **2019**, *9* (46), 26956–26960.
- (61) Zhao, S.; Bai, Y.; Chen, J.; Bai, A.; Gao, W. Optical and magnetic properties of copper doped zinc oxide nanofilms. *J. Mag.* **2014**, *19* (1), 68–71.
- (62) Tonelli, D.; Scavetta, E.; Gualandi, I. Electrochemical deposition of nanomaterials for electrochemical sensing. *Sensors* **2019**, *19* (5), 1186.
- (63) Pandit, B.; Goda, E. S.; Shaikh, S. F., Electrochemical deposition toward thin films. In *Simple Chemical Methods for Thin Film Deposition: Synthesis and Applications*; Springer: 2023; pp 245–304.
- (64) Theyagarajan, K.; Lakshmi, B. A.; Kim, Y.-J. Electrochemical Sensing of Acetaminophen in Biofluids, Pharmaceutical and Environmental Samples Using Cobalt Hexacyanoferrate Decorated Iron Terephthalate Metal Organic Framework. *Electrochim. Acta* **2024**, *488*, No. 144229.
- (65) Xie, C.; Li, H.; Niu, B.; Guo, H.; Lin, X. Comparison of ultrasonic vs mechanochemistry methods for fabrication of mixed-ligand Zn-based MOFs for electrochemical determination of luteolin. *J. Alloys and Comp.* **2024**, *989*, No. 174363.
- (66) Mondal, R.; Show, B.; Ahmed, S. F.; Mukherjee, N. Electrochemically selective detection of dopamine over serotonin by CuO/Cu<sub>2</sub>O bulk heterostructure electrode. *Bull. Mater. Sci.* **2024**, *47* (2), 62.
- (67) Yildiz, D. E.; Unal, F.; Taşaltın, N. Non-enzymatic electrochemical voltammetric sensors based on thulium: zinc oxide for dopamine detection. *J. Mater. Sci.: Mater. Electron.* **2024**, *35* (7), 475.
- (68) Alkahtani, S. A.; Mahmoud, A. M.; Ali, R.; El-Wakil, M. M. Sonochemical synthesis of lanthanum ferrite nanoparticle-decorated carbon nanotubes for simultaneous electrochemical determination of acetaminophen and dopamine. *Microchim. Acta* **2024**, *191* (1), 25.
- (69) Ahmed, J.; Faisal, M.; Algethami, J. S.; Alsaiari, M.; Harraz, F. A. A novel In<sub>2</sub>O<sub>3</sub>-doped ZnO decorated mesoporous carbon nanocomposite as a sensitive and selective dopamine electrochemical sensor. *J. Mater. Res. Technol.* **2024**, *29*, 540–549.
- (70) Xia, Y.; Li, G.; Zhu, Y.; He, Q.; Hu, C. Facile preparation of metal-free graphitic-like carbon nitride/graphene oxide composite for simultaneous determination of uric acid and dopamine. *Microchem. J.* **2023**, *190*, No. 108726.
- (71) Nurzulaikha, R.; Lim, H.; Harrison, I.; Lim, S.; Pandikumar, A.; Huang, N.; Lim, S.; Thien, G.; Yusoff, N.; Ibrahim, I. Graphene/SnO<sub>2</sub> nanocomposite-modified electrode for electrochemical detection of dopamine. *Sens. Bio-Sens. Res.* **2015**, *5*, 42–49.
- (72) Yang, Z.; Zheng, X.; Zheng, J. A facile one-step synthesis of Fe<sub>2</sub>O<sub>3</sub>/nitrogen-doped reduced graphene oxide nanocomposite for enhanced electrochemical determination of dopamine. *J. Alloys and Comp.* **2017**, *709*, 581–587.
- (73) Anbumannan, V.; Kumar, R. R.; Suresh, K. Enhanced electrochemical detection of dopamine by graphene oxide/tungsten trioxide nanocomposite. *Mater. Sci. Semicond. Process.* **2021**, *127*, No. 105696.
- (74) Zablocka, I.; Wysocka-Zolopa, M.; Winkler, K. Electrochemical detection of dopamine at a gold electrode modified with a polypyrrole-mesoporous silica molecular sieves (MCM-48) film. *Inter. J. Mol. Sci.* **2019**, *20* (1), 111.
- (75) Chittravathi, S.; Swamy, B. K.; Mamatha, G.; Sherigara, B. Electrochemical behavior of poly (naphthol green B)-film modified carbon paste electrode and its application for the determination of dopamine and uric acid. *J. Electroanal. Chem.* **2012**, *667*, 66–75.
- (76) Alsoghier, H. M.; Abd-ElSabour, M.; Alhamzani, A. G.; Abou-Krishna, M. M.; Assaf, H. F. Real samples sensitive dopamine sensor based on poly I, 3-benzothiazol-2-yl ((4-carboxylicphenyl) hydrazono) acetonitrile on a glassy carbon electrode. *Sci. Rep.* **2024**, *14* (1), 16601.